The mass and density of the dwarf planet (225088) 2007 OR$_{10}$

Csaba Kiss[a,*], Gábor Marton[a], Alex H. Parker[b], Will M. Grundy[c], Anikó Farkas-Takács[a,d], John Stansberry[e], Andras Pál[a,d], Thomas Müller[f], Keith S. Noll[g], Megan E. Schwamb[h], Amy C. Barr[i], Leslie A. Young[b], József Vinkó[a]

[a] Konkoly Observatory, Research Centre for Astronomy and. Earth Sciences, Hungarian Academy of Sciences, Konkoly Thege 15-17, H-1121 Budapest, Hungary
[b] Southwest Research Institute, Boulder, CO, USA
[c] Lowell Observatory, Flagstaff, AZ, USA
[d] Eötvös Lomnd University, Pázmány P. st. 1/A, 1171 Budapest, Hungary
[e] Space Telescope Science Institute, 3700 San Martin Dr., Baltimore, MD 21218, USA
[f] Max-Planck-Institutfur extraterrestrische Physik, Giesenbachstrasse, Garching, Germany
[g] NASA Goddard Space Flight Center, Greenbelt, MD 20771, USA
[h] Gemini Observatory, Northern Operations Center, 670 North A'ohoku Place, Hilo, HI 96720, USA
[i] Planetary Science Institute, 1700 E. Ft. Lowell, Suite 106, Tucson, AZ 85719, USA

ARTICLE INFO

ABSTRACT

The satellite of (225088) 2007 OR$_{10}$ was discovered on archival Hubble Space Telescope images and along with new observations with the WFC3 camera in late 2017 we have been able to determine the orbit. The orbit's notable eccentricity, $e \approx 0.3$, may be a consequence of an intrinsically eccentric orbit and slow tidal evolution, but may also be caused by the Kozai mechanism. Dynamical considerations also suggest that the moon is small, $D_{eff} < 100$ km. Based on the newly determined system mass of $1.75 \cdot 10^{21}$ kg, 2007 OR$_{10}$ is the fifth most massive dwarf planet after Eris, Pluto, Haumea and Makemake. The newly determined orbit has also been considered as an additional option in our radiometric analysis, provided that the moon orbits in the equatorial plane of the primary. Assuming a spherical shape for the primary this approach provides a size of 1230 ± 50 km, with a slight dependence on the satellite orbit orientation and primary rotation rate chosen, and a bulk density of 1.75 ± 0.07 g cm^{-3} for the primary. A previous size estimate that assumed an equator-on configuration $(1535_{-225}^{+75}$ km$)$ would provide a density of $0.92_{-0.14}^{+0.46}$ g cm^{-3}, unexpectedly low for a 1000 km-sized dwarf planet.

1. Introduction

Satellites are very important in studying the formation and evolution of Kuiper belt objects (see Noll et al., 2008, for a summary). The orbit of a satellite allows us to obtain accurate system mass and also density when the size of the main body is known (typically from radiometry or occultation measurements). Densities are also indicative of the internal structure, and are important constraints for satellite formation theories. It is possible that systems with small and large moons formed by different processes. Systems with large moons may have formed in low-velocity grazing collisions, both bodies retaining their original compositions and also the primordial densities.

Systems with small moons may have formed in collisions when low-density icy material is lost, increasing the bulk density of the primary (Barr and Schwamb, 2016).

The satellite orbits of most large KBO binaries are nearly circular. An exception is (50000) Quaoar, where the orbit of Weywot is moderately eccentric ($\epsilon = 0.14$), an orbital state that is likely not the consequence of a tidal evolution from an initially circular orbit. The long orbit evolution timescale obtained for Weywot indicates instead that it may have formed with a non-negligible eccentricity (Fraser et al., 2013).

The satellite of (225088) 2007 OR$_{10}$ (hereafter shortened to 2007 OR$_{10}$) was discovered on archival images obtained with the WFC3 camera of the Hubble Space Telescope (Kiss et al., 2017). This discovery completes the list of outer solar system dwarf planets with known satellites: now all bodies larger than ~1000 km in diameter are known to harbor moons (Pluto-Charon, Eris, Haumea, Makemake, Quaoar, Orcus). The existence of a satellite was originally suspected from the long rotation period (~44.8 h) derived from a Kepler-K2 multi-day

---

* Corresponding author.
  E-mail address: kiss.csaba@csfk.mta.hu (C. Kiss).

Table 1

Relative astrometry (J2000) and photometry of the satellite with respect to 2007 OR$_{10}$. The first two lines correspond to the discovery epochs (see Kiss et al., 2017), the next four lines represent the results of the HST recovery observations in 2017. δr_p and δr_r are the astrometry residuals (R.A. and DEC combined) from the best fit prograde and retrograde model as presented in Table 2 and Fig. 1. Note that the HST/WFC3 pixel scale is ~40 mas.

MJD start	MJD end	$\Delta\alpha$	$\Delta\delta$	Filter	Δm	δr_p	δr_r
		(mas)	(mas)		(mag)	(mas)	
55,141.71282	55,141.72189	$+13 \pm 4$	-452 ± 2	F606W/F814W	$4.42 \pm 0.21/4.35 \pm 0.25$	5	4
55,457.66116	55,457.66987	-219 ± 3	$+127 \pm 6$	F606W/F775W	$4.15 \pm 0.13/4.43 \pm 0.30$	1	4
58,029.66532	58,029.68957	-165 ± 8	$+153 \pm 15$	F606W	4.93 ± 0.30	18	28
58,037.34117	58,037.36635	-258 ± 7	-405 ± 5	F814W	5.01 ± 0.15	8	3
58,044.22969	58,044.25393	$+130 \pm 2$	-365 ± 3	F606W	4.65 ± 0.15	1	2
58,092.23763	58,092.26689	-15 ± 6	-448 ± 2	F606W	4.64 ± 0.17	3	2

light curve (Pál et al., 2016). The initial discovery was based on observations at two epochs only, therefore the orbit of the satellite could not be derived unambiguously from these data alone.

Here, we report on successful recovery observations of the satellite of 2007 OR$_{10}$, taken with the WFC3 camera of the Hubble Space Telescope (HST) in 2017. The observations allow us to determine the orbit sufficiently well to obtain system mass and estimate the density of the primary. We also give a short assessment of possible orbital evolution and the consequences for both the primary and the satellite.

2. Observations and data analysis

New observations of 2007 OR$_{10}$ were obtained with HST in the framework of the proposal "The Moons of Kuiper Belt Dwarf Planets Makemake and 2007 OR$_{10}$" (proposal ID: 15207, PI: A.H. Parker) at four epochs in October and December 2017 (see Table 1). The WFC3/UVIS camera system with the UVIS2-C512C-SUB aperture was used to take multiple exposures, alternating between the F350LP and either the F606W or the F814W filters. We created co-added images in the co-moving frame of 2007 OR$_{10}$ using images obtained with the same filters. The satellite was clearly visible and well-separated from 2007 OR$_{10}$ on the images taken on October 10, 18 and December 5, but was quite close to the bright primary on October 3. We used point-spread function (PSF) subtracted images to perform astrometry and photometry of the satellite, using the same DAOPHOT-based routines as in (Kiss et al., 2017). The model PSFs used for subtraction were created using the TinyTim (Krist et al., 2010) software, using specific setups (date, camera system, target's pixel position, focal length).

The results are summarized in Table 1 and Fig. 1. Due to the proximity of the satellite and the primary, the astrometry of the 2017 October 3 measurement has a notably higher uncertainty than the other measurements. While in the other cases, the images with and without PSF-subtraction provided nearly identical astrometry (< 1 mas), these differences are an order of magnitude larger at the October 3 epoch (> 10 mas) that is also reflected in the quoted astrometric uncertainties.

3. Orbit fitting

After the October 2017 observations, we generated a collection of thousands of orbits consistent with the ensemble of astrometric data, using Monte Carlo procedures (Grundy et al., 2008). This cloud of orbits provided a representation of the probability distribution in orbital element space. It contained a number of dense clumps corresponding to distinct orbit solutions differing in their orbital periods, eccentricities, semi-major axes, etc. Each clump was used to provide initial parameters for a least-squares fit, using the Ameoba downhill simplex algorithm (Nelder and Mead, 1965; Press et al., 1992) to adjust the orbital elements to minimize the residuals between observations and predicted positions. We chose December 2017 as the optimal time for the last observation because the cloud of possible orbits was well dispersed, but
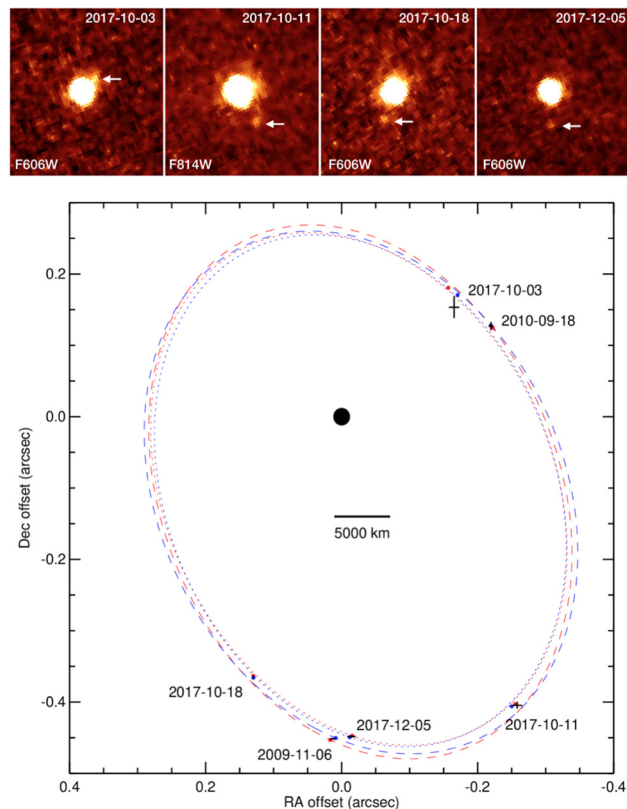

Fig. 1. *Upper panel:* Hubble Space Telescope WFC3/UVIS images of 2007 OR$_{10}$, obtained in October–December 2017 recovery observations (see Table 1 for details). *Lower panel:* Sky-projected orbit of the satellite around 2007 OR$_{10}$. Dashed lines correspond to the orbit at the time of the 2009 observation and the dotted ones are at the time of the recovery observations in 2017. The blue ellipse corresponds to the prograde, red one to the retrograde solution. The points with error bars mark the observed positions of the satellite (see Table 1) while the small blue and red points mark the expected relative positions at the time of the observations, derived from the orbital solutions. The points marking the satellite are sized to 100 km radius, while that of 2007 OR$_{10}$ (in the center) corresponds to a diameter of 1535 km. (For interpretation of the references to color in this figure legend, the reader is referred to the web version of this article.)

not homogeneous, when projected on the sky plane at that epoch. After completion of the final observation, the Monte Carlo orbit fits were repeated, and all but one of the clumps of potential orbits were rejected, leaving only the solution in Table 2 and also illustrated in Fig. 1.

This pole solution has two counterparts, mirrors of one another through the sky plane at the time of the 2017 observations. To distinguish which of the prograde and retrograde solutions is the correct one will require waiting for (225088) 2007 OR$_{10}$ to move further along its heliocentric orbit, enabling Earth-based observers to view the system

Table 2
Orbital solutions and derived parameters from the HST observations. The orbital elements correspond to the epoch of 2457000.0 (JD).

	Prograde	Retrograde
P (day)	25.22073 ± 0.000357	25.22385 ± 0.000362
a (km)	24,021 ± 202	24,274 ± 193
e	0.2908 ± 0.0070	0.2828 ± 0.0063
i (deg)	83.08 ± 0.86	119.14 ± 0.89
ϵ (deg)	205.57 ± 0.95	294.47 ± 1.38
Ω (deg)	31.99 ± 1.07	104.09 ± 0.82
ϖ (deg)	109.05 ± 1.88	199.15 ± 1.67
M_{sys} (kg)	$(1.726 \pm 0.043) \cdot 10^{21}$	$(1.781 \pm 0.043) \cdot 10^{21}$
α_{pole} (deg)	301.990 ± 1.021	14.096 ± 0.679
δ_{pole} (deg)	6.914 ± 0.451	−29.143 ± 0.408
λ_{pole} (deg)	305.972 ± 1.160	0.098 ± 0.723
β_{pole} (deg)	26.447 ± 0.550	−32.101 ± 0.516
i_{helio} (deg)	51.828 ± 0.829	129.050 ± 0.703

from a different direction. But already, the period and semi-major axis are reasonably well determined, enabling us to derive the system mass. Additionally, the eccentricity is significantly non-zero ($e = 0.29$ and 0.28 in the prograde and retrograde cases, respectively), a result that we explore in more detail below. The prograde and retrograde solutions provide a mean mass estimate of $1.75 \pm 0.07 \cdot 10^{21}$ kg, which is the fourth largest known mass among dwarf planets after Eris, Pluto and Haumea (Brown and Schaller, 2007; Ragozzine and Brown, 2009; Stern et al., 2015, respectively). This mass is very similar to that of Charon ($1.586 \cdot 10^{21}$ kg; Nimmo et al., 2017).

The small residuals of the individual astrometry points (Fig. 1) and the observed change between the apparent orbits of the satellite in the first (2009/10) and second (2017) observing seasons agree well with the assumption that the binary orbit is stable, i.e. the orbit pole did not change between the two observational seasons, and the change of the apparent orbit of the satellite can be explained by the aspect angle change due to the displacement of 2007 OR_{10} on its heliocentric orbit. The largest, 1.6 σ residual is between the model and observed positions of the October 3, 2017 measurement; in the other cases, it is ~ < 1 σ.

4. Photometry results and colors

Based on the differential photometry of 2007 OR_{10} and the satellite (see Table 1) we obtained average brightness differences of $\Delta(F606W) = 4.^{m}68 \pm 0.^{m}11$ (observations on October 3, 18, and December 5) and $\Delta(F814W) = 5.^{m}01 \pm 0.^{m}30$ (October 11). We use a system-integrated absolute brightness of $H_V = 2.34 \pm 0.01$ and the color V–I = 1.65 ± 0.03 (Boehnhardt et al., 2014) to obtain absolute brightness values for the satellite from the relative photometry. When transforming the HST/

WFC3 photometry to the Johnson-Cousins system (F606W to V and F814W to I) we applied a V band correction of $0.^{m}10$ due to the color difference of the satellite and the primary; in the case of the I-band brightness values the correction was much smaller ($< 0.^{m}003$) (see Sahu et al., 2017, for the transformations between the HST/WFC3 and the Johnson-Cousins photometric systems). For the absolute brightness and color of the satellite, we obtained $H_V{}^s = 6.93 \pm 0.15$ and $(V - I)_s = 1.22 \pm 0.17$, i.e. it is somewhat less red than the primary. From this color, a spectral slope of $S_s{}' = 19 \pm 7\%/(1000 \,\text{Å})$ can be derived, while the spectral slope of the notably redder primary is $S_p{}' = 42 \pm 2\%/(1000 \,\text{Å})$.

Mid-sized trans-Neptunian binaries typically have nearly equal colors (Benecchi et al., 2009), indicating that in most cases the satellite co-formed in a locally homogeneous, but globally heterogeneous protoplanetary disk. For larger bodies, however, color differences of $0.^{m}2$–$0.^{m}3$ are common, as it is the case for Pluto-Charon (Grundy et al., 2016), Eris-Dysnomia (Brown and Schaller, 2007) or Orcus-Vanth (Brown et al., 2010). In the latter two cases, the primaries have nearly solar colors and the satellites are redder and darker, however, in these cases the colors of the primaries may not be original. The 2007 OR_{10} system seems to have the largest color difference among trans-Neptunian binaries, with $\Delta(V–I) = 0.43 \pm 0.17$.

5. Radiometric size estimates

The thermal emission of 2007 OR_{10} was observed with the PACS camera of the Herschel Space Observatory, and these data were analysed in detail in Pál et al. (2016). Both the Near-Earth Thermal Asteroid Model and the thermophysical model (TPM) pointed to a same best-fit size of $1535_{-225}{}^{+75}$ km. In that paper, two TPM configurations were tested: a pole-on and an equator-on, and the latter one gave the best fit to the observed flux densities. Although the recent HST observations do not constrain the rotation axis orientation directly, one may assume that the orbit of the satellite is in the equatorial plane of 2007 OR_{10} and use our two pole orientations for the spin axis of the primary. Overall, we considered four possible pole orientations, presented in Table 3. We allowed thermal inertias in the range of $\Gamma = 0.1$–$50 \,\text{J m}^{-2}\,\text{s}^{-1/2}\,\text{K}^{-1}$, and a constant emissivity of $\epsilon = 0.9$ in the TPM models. As was recently demonstrated (Fornasier et al., 2013; Lellouch et al., 2017), far-infrared and submillimetre flux densities of outer solar system objects may be affected by lower-than-unity relative emissivities with respect to those in the mid-infrared regime. While this is most expressed in the submillimetre, a slight deviation in relative emissivity ($\epsilon_{rel} \approx 0.9$) was also observed at 160 μm for some objects. If the emissivity of 2007 OR_{10} were depressed at 160 μm that would affect our derived diameter; however, the data show no indication of such an

Table 3
Thermophysical models setups with different rotational axis orientations, represented by the ecliptic coordinates of the rotational pole (λ_p, β_p), and by the subsolar latitude β_{ss}. We also show the corresponding best fit TPM solution of effective diameter D_{eff}, geometric albedo p_V, thermal inertia Γ and the density of the primary derived from these values. Comments: eon — equator-on; pon — pole-on; pg/rg — prograde/retrograde satellite in the equatorial plane of the primary; s — spherical; e — tidally distorted ellipsoid.

Case	λ_p	β_p	β_{ss}	P_{rot}	Comment	D_{eff}	p_V	Γ	ρ
	(deg)	(deg)	(deg)	(h)		(km)		(J m^{-2} s$^{-1/2}$ K^{-1})	(g cm^{-3})
1	331.9	86.7	0	44.8	eon/s	1531	0.09	3	$0.92_{-0.14}{}^{+0.46}$
2	331.9	−3.3	90	–	pon/s	1158 ± 32	0.16 ± 0.01	Unconstrained	2.15 ± 0.17
3a	306.0	26.4	51	44.8	pg/s	1224 ± 55	0.14 ± 0.01	1–5	1.80 ± 0.16
3b	306.0	26.4	51	22.4	pg/s	1238 ± 50	0.14 ± 0.01	1–5	1.74 ± 0.16
3c	0.1	−32.1	51	44.8	rg/s	1227 ± 56	0.14 ± 0.01	1–5	1.79 ± 0.16
3d	0.1	−32.1	51	22.4	rg/s	1241 ± 50	0.14 ± 0.01	1–5	1.73 ± 0.16
4	331.9	86.7	0	44.8	eon/e	1549	0.09	3	$0.89_{-0.14}{}^{+0.44}$
5a	306.0	26.4	51	44.8	pg/e	1155 ± 52	0.16 ± 0.01	1–5	2.13 ± 0.17
5b	306.0	26.4	51	22.4	pg/e	1169 ± 47	0.16 ± 0.01	1–5	2.07 ± 0.17
5c	0.1	−32.1	51	44.8	rg/e	1158 ± 53	0.16 ± 0.01	1–5	2.13 ± 0.17
5d	0.1	−32.1	51	22.4	rg/e	1172 ± 47	0.15 ± 0.01	1–5	2.05 ± 0.17

effect for 2007 OR$_{10}$.

Due to its large size, it is not expected that the shape of 2007 OR$_{10}$ would deviate significantly from a sphere. For a rotating body with relatively low angular velocity the expected shape is a Maclaurin spheroid with semi-major axes $a = tb > c$, and rotation around the c axis (Plummer, 1919). The flattening ($\epsilon = 1 − c/a$) can be calculated for a specific normalized angular velocity of $\omega^2/\pi G\rho$, and for $\rho = 1 \, g \, cm^{-3}$ we obtained $\epsilon = 0.03$ and $\epsilon = 0.007$ for $P = 22.4 \, h$ and 44.8 h, respectively. This is very far from the fast rotator cases when the equilibrium configuration is a Jacobi ellipsoid. As $a = b$ for a Maclaurin ellipsoid, this shape results in a flat light curve.

Charon has a mass very similar to that of 2007 OR$_{10}$, $m_{Ch} = 1.586 \cdot 10^{21} \, kg$, and its shape is very close to a sphere, with $a = 606 ± 1 \, km$ and flattening $< 0.5\%$ (Nimmo et al., 2017), despite the presence of Pluto. This suggests that the observed light curve is likely caused by surface features (albedo variegations) rather than by a distorted shape in the case of 2007 OR$_{10}$, too. Therefore, we consider a sphere for 2007 OR$_{10}$ in the thermal modelling as the main shape option.

However, one may eventually assume that we see a distorted body with $a > b > c$ that leads to the observed light curve. A tidally distorted body would have $(a–b) = 4(b–c)$; for the equator-on and prograde/retrograde equatorial satellite cases the observed light curve amplitude of $\Delta m = 0.^m09$ (Pál et al., 2016) requires $b = 0.92$ and $b = 0.74$ (Cases 4 and 5a…d). For the thermal emission here, we assume that we observed ten at a 'mean' rotational phase. In these cases, the estimated effective diameters are different from those in the corresponding spherical cases due to the different projected area, leading to different effective diameters and densities as well.

As input for the thermophysical model calculations we used the 70, 100 and 160 μm flux densities presented in Pál et al. (2016), a rotation period of $P_{rot} = 44.81 \, h$ or the half period, $P = 22.4 \, h$ (Pál et al., 2016), a low to intermediate surface roughness (0.1–0.3 r.m.s. of surface slopes), and an absolute magnitude of $H_V = 2.^m34 ± 0.^m05$ (Boehnhardt et al., 2014).

As was shown in Kiss et al. (2017), the satellite can noticeably contribute to the thermal emission only if its surface is very dark ($p_V < 4\%$). As we argue later in the this paper, dynamical considerations strongly favour a small satellite with $p_V > 20\%$ therefore the satellite's contribution is negligible in the thermal emission models.

The best fit to the data is given by the Case-1 (equator-on, subsolar latitude of $\beta_{ss} \approx 0°$) configuration (reduced $\chi^2 \approx 0.1$), resulting in $\Gamma = 2–6 \, J \, m^{-2} \, s^{-1/2} \, K^{-1}$, with an optimum solution of $\Gamma = 3$ it, $D_{eff} = 1531 \, km$, and $p_V = 0.09$.

Lellouch et al. (2013) obtained $\Gamma = 2.5 ± 0.5 \, J \, m^{-2} \, s^{-1/2} \, K^{-1}$ for typically 100 km-sized objects observed at heliocentric distances of $r_h = 20–50 \, AU$. At the distance of 2007 OR$_{10}$, the thermal inertia of a similar surface would be lower due to the lower surface temperatures: assuming that the T^3 term dominates in the thermal conductivity, thermal inertia scales.

as $\propto r_h^{-3/4}$ (Delbo et al., 2015), i.e. a Γ of a factor of ~ 2 lower is expected at the distance of 2007 OR$_{10}$.

The thermal inertia of larger bodies, however, may be notably larger. Lellouch et al. (2011, 2016) obtained $\Gamma_{Pl} = 16–26 \, J \, m^{-2} \, s^{-1/2} \, K^{-1}$ and $\Gamma_{Ch} = 9–14 \, J \, m^{-2} \, s^{-1/2} \, K^{-1}$, for Pluto and Charon, respectively.

These high Γ values are thought to be caused by the slow rotation, and the $\propto P^{1/2}$ dependence of the diurnal skin depth on the rotation period. 2007 OR$_{10}$ rotates faster than Pluto and Charon (6.38 d orbital/ rotation period of Pluto-Charon versus 44.8 h), but still much slower than a typical trans-Neptunian object ($P = \sim 6–12 \, h$).

For 2007 OR$_{10}$, this suggests a factor of ~ 2 reduction of Γ compared with Pluto or Charon, altogether a factor of ~ 4 smaller values, considering the r_h dependence as well. This gives $\Gamma = 4–6 \, J \, m^{-2} \, s^{-1/2} \, K^{-1}$ for 'Pluto-like', and $\Gamma = 2.2–3.5 \, J \, m^{-2} \, s^{-1/2} \, K^{-1}$ for 'Charon-like' surfaces, in a very good agreement with that obtained from the

thermophysical model analysis assuming Case-1 (equator-on). The analysis of the thermal emission of a Haumea also indicates a similarly high thermal inertia (Müller et al., 2018).

The pole-on configuration (Case 2, $\beta_{ss} \approx 90°$) provides a size of $D_{eff} = 1158 ± 32 \, km$, and this value is independent of the thermal inertia chosen. Pál et al. (2016) found a peak-to-peak light curve amplitude of $\Delta m = 0.^m09$, which in the case of a near-to-pole-on configuration would be a significantly supressed fraction of a much larger intrinsic light curve amplitude that would be seen at low obliquity. $\Delta m = 0.^m09$ associated with $\beta_{ss} > 80°$ would require an extremely elongated body (not expected due to the slow rotation) or a very high (a factor of ~ 2 or larger) variation in reflected light and therefore also in geometric albedo on the surface of a more or less spherical body. Such large variations are seen e.g. on the surface of Pluto (Bond albedo of $A = 0.2–0.9$) and also on Charon ($A = 0.1–0.5$), as revealed by New Horizons (Buratti et al., 2017).

In the case of the coincident orbital/rotational axes configurations (Cases 3a…3d) and 4, $\beta_{ss} \approx 51°$) the dependence of the final solution on the thermal inertia chosen is relatively weak, and it cannot be well constrained by the far-infrared flux densities. The error bars of the observed flux densities allow acceptable solutions for these pole orientations as well: for these cases, we obtained $D_{eff} = 1224 ± 55 \, km$ and 1238 ± 50 km for the prograde solution for $P = 44.8 \, h$ and 22.4 h (3a and 3b), and $D_{eff} = 1227 ± 56 \, km$ and 1241 ± 50 km for the retrograde cases with $P = 44.8 \, h$ and 22.4 h (3c and 3c), assuming Charon-like inertias. The similar sizes obtained show that (i) the effect of prograde/retrograde rotation is negligible for the thermal emission calculations and (ii) that the application of the slower/faster rotation introduces an uncertainty of $\sim 1\%$ in the estimated size and a corresponding $\sim 3\%$ uncertainty in volume and density (see below). Higher thermal inertias of a 'Pluto-like' surface provide D_{eff} and p_V even closer to that of the Case 1 solution. In these cases, the observed $\Delta m = 0.^m09$ light curve amplitude can be explained e.g. by a large, $\sim 60°$-radius darker/brighter equatorial area with an albedo contrast of $\sim 17\%$ over the global value ($\Delta p_V \approx 2\%$ on the absolute scale), seen under the observed orbital inclination.

Considering a tidally distorted ellipsoid compatible with the observed light curve (Cases 4 and 5a…5d) leads to somewhat different effective radii. In the equator-on case, this leads to $D_{eff} = 1549 \, km$, slightly ($\sim 1\%$) larger than the corresponding spherical solution (Case 1). In the ellipsoidal pro-/retrograde equatorial satellite cases (5a…5b), however, the effective diameters obtained are typically $\sim 6\%$ smaller ($\sim 1160 \, km$) than in the spherical cases (3a…3d). The difference between the orbit solution and rotational period variations are, again, small, $\sim < 1\%$.

In all the cases above χ_r^2 1, i.e. all these thermal emission solutions are acceptable for 2007 OR$_{10}$.

6. The density of 2007 OR$_{10}$

To calculate the density from the mass of $1.75 ± 0.07 \cdot 10^{21} \, kg$, we first used $D_{eff} = 1535_{-225}^{+75} \, km$, derived from radiometric models by Pál et al. (2016), corresponding to our best-fit, Case-1 (equator-on) TPM solution. This provides an average density estimate of $0.92_{-0.14}^{+0.46} \, g \, cm^{-3}$, assuming a spherical body. Using the effective diameters from the Case-3a-d TPM solutions (satellite orbit in equatorial plane), the density is $\rho = 1.74 ± 0.16 \, g \, cm^{-3}$. The highest density, $\rho = 2.15 ± 0.17 \, g \, cm^{-3}$, is obtained for the pole-on (Case-2) solution. As was pointed out above, the triaxial ellipsoid cases (4, 5a–d) are a very unlikely option for a massive and slow rotating Kuiper belt object like 2007 OR$_{10}$.

We compare the density of 2007 OR$_{10}$ with other trans-Neptunian object in Fig. 2. Considering the best-fit size (Case-1, red symbol and red arc in Fig. 2), the density of 2007 OR$_{10}$ is significantly lower than that of other objects with similar sizes, and rather similar to Kuiper belt object densities in the 500–1000 km range. This would point to the
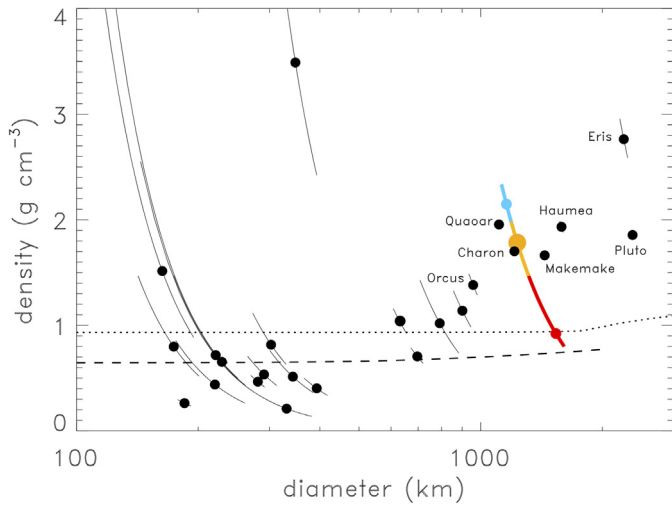
Fig. 2. Densities of trans-Neptunian objects as a function of their diameters. Majority of the data is taken from Table 2 in Kovalenko et al. (2017), but using the latest data for Haumea (Ortiz et al., 2017), Pluto and Charon (Stern et al., 2015), and for G!kún‖'hòmdímà (Grundy et al., 2018). Color symbols/arcs represent different densities obtained for 2007 OR$_{10}$ from the thermophysical model results: blue arc — pole-on solution; orange arc — satellite orbit in the equatorial plane of the primary; red arc — equator-on solution. The dotted and dashed curves represent the density of a pure water ice sphere (Lupo and Lewis, 1979), and the density expected from granular ice with self-compression (McKinnon et al., 2005), respectively. (For interpretation of the references to color in this figure legend, the reader is referred to the web version of this article.)

highest ice/lowest rock fraction among the large Kuiper belt objects. The density of ~0.92 g cm^{-3} is, however, consistent with the density of a pure water ice sphere (see Fig. 2). Such a low bulk density may also be a consequence of a core with a typical mixture of rock and ice (inside ~50% of the radius) and a highly porous mantle, where the low internal pressures may allow a porosity much higher (up to ~50%) than the residual porosities in the core (~10%), as discussed e.g. for Quaoar in McKinnon et al. (2008).

The Case-3a–d solutions ($\rho = 1.74 \pm 0.16$ g cm^{-3}), put 2007 OR$_{10}$ in the range of densities defined by Charon, Haumea, Makemake, Orcus and Quaoar (orange symbol and arc in Fig. 2). Densities in this range are expected from the largest Kuiper belt objects if their moons are formed in collisions in which the primary retained its original composition and its primordial density (Barr and Schwamb, 2016).

The high density obtained for the pole-on configuration (Case-2, $\rho = 2.15 \pm 0.17$ g cm^{-3}, blue symbol and arc in Fig. 2) is already in the range in which present day densities may have been caused by more energetic collisions, leading to a significant loss of ice. Again, this configuration is not very likely, due to the existence of a visible range light curve (Pál et al., 2016). The present accuracy of the radiometric size determination of 2007 OR$_{10}$ alone does not allow us to unambiguously choose between the possibilities presented above. However, considering all constraints, including the densities derived above, the most plausible solution for 2007 OR$_{10}$ seems to be a spherical shape with a single-peaked visible range light curve ($P = 22.4$ h) caused by albedo variegations, and co-planar primary equator and satellite orbit. This corresponds to the thermal emission solutions 3b and 3d.
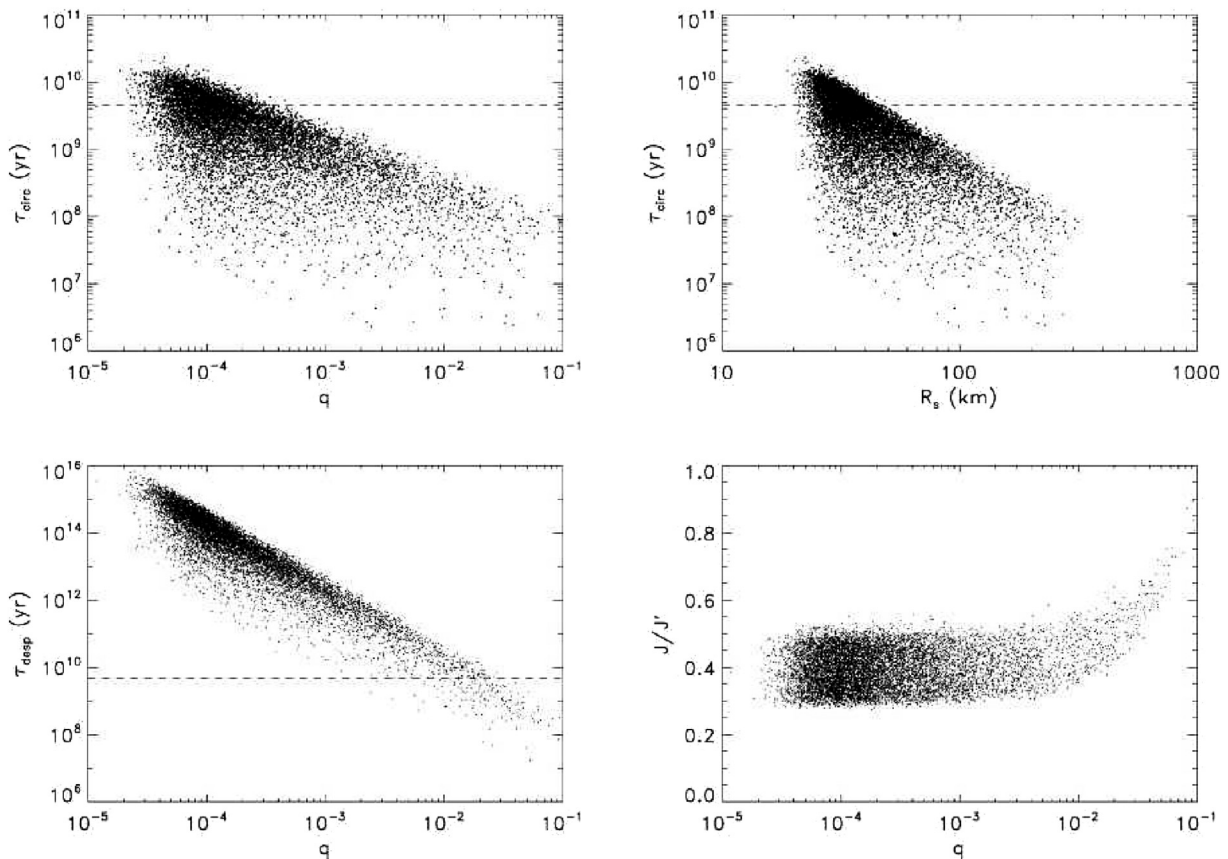

Fig. 3. *Top-left*: orbit circularization timescales, τ_{circ} vs. satellite to primary mass ratio (q); *Top-right*: τ_{circ} vs. the effective radius of the satellite (R$_S$); *Bottom-left*: Despinning timescale vs. q of the primary; *Bottom-right*: Normalized angular momentum (J/J') vs. q. The dashed horizontal line represents the age of the Solar system on those figures where timescales are plotted.

7. Formation and tidal evolution

To investigate the possible formation scenarios and the dependence of the tidal evolution on the basic properties of the system we considered a large number of configurations covering the possible size, density and structural properties of both the primary and the satellite, and estimated the tidal time scales and other parameters in a Monte-Carlo manner.

Variables with known values are assumed to have a normal distribution with expectation value and standard deviation equal to their obtained values and uncertainties. These include the parameters of the satellite's orbit (semi-major axis, eccentricity) and also the properties that are directly derived from these parameters (system mass). The absolute magnitude of the primary and satellite are modelled in the same way ($H_V = 2.34 \pm 0.01$ and 6.93 ± 0.15, respectively).

In the case of variables with no known constraints, we apply a feasible range of parameters and pick a specific value randomly. The geometric albedo of the satellite is chosen from $p_V = 0.01–1.0$, and the effective radius is obtained from the absolute magnitude and p_V assumed. We used the effective diameter range of 1126 to 1610 km for the main body, as given in Section 5.

We estimated the orbit circularization timescale (τ_{circ}) of the system following Noll et al. (2008), Eq. 8, and a tidal dissipation factor Q was assumed in the range of 10–500 (see e.g. Farinella et al., 1979; Goldreich and Soter, 1966). The obtained τ_{circ} values are plotted in Fig. 3.

As the system has a notable eccentricity, τ_{circ} should at least be larger than the age of the Solar system, assuming that the binary system formed 4.5 Gyr ago, either by major impact or capture. The only configurations that fulfill this requirement are those for which $q < 4 \cdot 10^{-4}$ or $R_S = 18–50$ km, corresponding to geometric albedos of $p_V = 1.0–0.2$. For these configurations, the tidal factor must also be large, $Q > 100$ in all cases, in agreement with that found e.g. for the icy satellites of the giant planets (Goldreich and Soter, 1966). Small tidal factors would result in a faster orbital evolution, not compatible with the observed moderate eccentricity.

Similarly, the spin-locking or despinning timescale, τ_{desp}, can also be estimated for both the primary and the satellite, using Eq. 9 in Noll et al. (2008). The τ_{desp} is below 10^7 yr for all of our model configurations, i.e. the rotation of the satellite is almost certainly tidally locked. For the primary, however, these timescales are much longer. τ_{desp} is below 4.5 Gyr only when $q > 2 \cdot 10^{-2}$. This large q would, on the other hand, lead to a fast circularization of the orbit that obviously did not happen. $\tau_{desp} > 10^{12}$ yr for the system parameters allowed by the observed eccentricity.

The tidal despinning timescales derived above strongly suggest that the observed light curve can be attributed to the primary. As suggested in Pál et al. (2016), the observed rotation period may be the orbital period of two nearby, tidally locked bodies. Knowing the system mass we can calculate the separation of such a semi-contact binary. In this case, the separation of the two bodies would be 4250 km or 67 mas. We investigated the co-added images of each observational epoch to identify any deviation from a single-source point spread function (PSF). Model PSFs were created using the TinyTim (Krist et al., 2010) software applied on two point sources with the expected separation and a range of relative brightnesses (1:2 to 1:20). A comparison of the model and observed PSFs show no signs of notable distortion at any of the 2017 epochs, down to the brightness ratio of 1:10 at which a double system would still be detectable.

We calculated the normalized angular momentum of the system (J/J' Noll et al., 2008), considering the combined spin and orbital angular momentum, for a wide range of system parameters. The dependence of J/J' on the primary to satellite mass ratio q is presented in Fig. 3. For smaller q values J/J' converges to ~ 0.4 (very close to that of Pluto-Charon), and despite that it decreases towards larger satellite masses it remains J/J' < 0.8 even for the largest q-s. As discussed in Noll et al.

(2008) binary systems produced by single collisions should have J/J' < 0.8, a condition that is fulfilled by the 2007 OR$_{10}$ system.

The evolution of the satellite orbit may be governed by the Kozai mechanism in the case of 2007 OR$_{10}$, due to perturbations by the Sun (for a detailed discussion of the Kozai mechanism and its implications for trans-Neptunian binaries, see Perets and Naoz, 2009). The inclination of the satellite orbit to the heliocentric orbit, i_h, is 51.°83 (prograde) or 129.°05 (retrograde). Because, in the quadrupole approximation, $\sqrt{1 - e^2} \cos i_h$ is conserved (Naoz, 2016), the possible ranges of eccentricity and inclination that the system may take are $0 \le e \le 0.65$ and $39° \le i_h \le 54°$ for prograde, and $0 \le e \le 0.63$ and $127° \le i_h \le 141°$ for retrograde orbit, with an associated timescale of $\sim 2 \cdot 10^6$ yr (see Eq. 1 in Perets and Naoz, 2009). Assuming that the present orbit is a consequence of the Kozai mechanism, and the system originally had an eccentricity close to zero, the initial inclination should have been $i_0 \approx 54°$. As the orbit of the satellite is not circularized, we may also put constraints on the strength of the combined Kozai and tidal effects (Perets and Naoz, 2009). For an initial inclination of $i_0 \approx 54°$, a system with orbital semi-major axis to characteristic tidal distance ratio of $a/r_c \le 1.5$ should have evolved to $e \approx 0$ by now, i.e. a nearly circular orbit. The a/r_c value depends primarily on q, and $e \gtrapprox 0$ requires $q \le 5 \cdot 10^{-3}$, obtained using the same approach as discussed in the case of the tidal timescales. This upper limit for q is in agreement with those obtained from other tidal timescale calculations above.

Irregularly shaped bodies have higher order terms in their gravitational potential which may dominate over the solar tides, the latter one responsible for the Kozai oscillations (Grundy et al., 2011; Nicholson et al., 2008). The most important quadrupole term is related to the flattening, ϵ, of the main body through the J$_2$ dynamic form factor. Assuming a Maclaurin ellipsoid – flattening due to rotation of a body with homogeneous internal density distribution – we can estimate the flattening of 2007 OR$_{10}$, following Plummer (1919). This results in flattening values of $0.0026 \le n \le 0.0118$, assuming a range of sizes and densities as in the calculation of the other dynamical timescale above. The corresponding form factors are in the range of $0.0001 \le J_2 \le 0.04$ (e.g. Essén, 2014). We calculated the critical semi-major axis a_c between the oblateness-dominated and solar-tide-dominated dynamics (e.g. Eq. 3 in Nicholson et al., 2008) and obtained $0.35 \le a/a_c \le 0.49$, where a is the semi-major axis of the satellite orbit in the 2007 OR$_{10}$ system. This suggests that dynamics of 2007 OR$_{10}$'s satellite should be governed by the oblateness of the primary, and not by solar tides, at least based on the present orbit. The associated precession timescales are $5.4 \cdot 10^4 \le \tau_p \le 4.2 \cdot 10^5$ yr for the prograde and $1.8 \cdot 10^4 \le \tau_p \le 1.4 \cdot 10^5$ yr for the retrograde case. Grundy et al. (2011) obtained a/a_c ratios for 17 trans-Neptunian binary systems, and in this sample there are only three systems (1999 OJ$_4$, (123509) 2000 WK$_{183}$, (66652) Borasisi) where the calculated a/a_c ratio is so low that that system is almost certainly in the oblateness-dominated regime. For 2007 OR$_{10}$, an oblateness-dominated dynamics should have led to a circularized orbit.

8. Conclusions

In most of the calculations above, 2007 OR$_{10}$'s satellite must be small in order to keep the satellite orbit from circularization during the lifetime of the solar system. While other mechanisms may play a role and increase the eccentricity from a small value to the presently observed one, a small satellite ($R_s < 50$ km) with a relatively bright surface ($p_V > 0.2$) would be consistent with all possible evolutionary scenarios. Among the largest Kuiper belt objects, Quaoar and Haumea have similarly small satellites and low relative mass ratios (Barr and Schwamb, 2016); the small satellites of Pluto also show high albedo values (Weaver et al., 2016). With respect to orbital characteristics, 2007 OR$_{10}$'s satellite is similar to Weywot that also has an eccentric orbit around Quaoar ($e \approx 0.14$, Fraser et al., 2013). An even smaller

satellite, with a mass ratio of $q \leq 5 \cdot 10^{-3}$, however, is not likely to have been able to slow down the rotation of the primary to the present ∼45 h, if it originally had a rotation period typical for a Kuiper belt object (8.6 h (Thirouin et al., 2014)).

The present accuracy of the radiometric size determination of 2007 OR_{10} does not allow us to unambiguously choose between the possible densities. The solution depends mainly on the orientation of the spin axis — a larger subsolar latitude, β_{ss}, leads to a smaller size and a higher density. Due to current large heliocentric distance and the cold surface temperatures, measurements in the mid-infrared range (∼10 – 25 μm) would not significantly improve the radiometric models (see the thermal emission modelling in Pál et al., 2016). An eccentricity $\epsilon \approx 0$ would make the equatorial plane satellite orbit significantly more likely, but the present orbit does not allow us to draw a definite conclusion on the relative positions of the two planes. Future occultation measurements and/or direct imaging e.g. by the James Webb Space Telescope may be able to reveal the true size and decide on the density.

Our simple dynamical considerations could not reveal the mechanism that could have led to the present orbit. In one possible scenario the satellite of 2007 OR_{10} could initially be a captured satellite in a distant orbit, where the Kozai mechanism pumped the eccentricity until tidal evolution took over, and finally this tidal dissipation shrank the orbit to an oblateness-dominated regime. In this regime, the noncircularized orbit may be explained, if the mass of the satellite is really small, as it is indicated by the dynamical timescale calculations above. More complex scenarios like the involvement of spin-orbit resonances may also lead to the present orbit. A more detailed analysis of the dynamics of 2007 OR_{10}'s satellite and its possible origin and evolution will be performed in a forthcoming paper.

Acknowledgements

References

Barr, A.C., Schwamb, M.E., 2016. Interpreting the densities of the Kuiper Belt's dwarf planets. Mon. Not. R. Astron. Soc. 460, 1542–1548.

Benecchi, S.D., Noll, K.S., Grundy, W.M., Buie, M.W., Stephens, D.C., Levison, H.F., 2009. The correlated colors of Transneptunian binaries. Icarus 200, 292–303.

Boehnhardt, H., Schulz, D., Protopapa, S., Götz, C., 2014. Photometry of Transneptunian objects for the Herschel key program 'TNOs are cool'. Earth Moon Planet. 114, 35–57.

Brown, M.E., Schaller, E., 2007. The mass of dwarf planet Eris. Science 316, 1585.

Brown, M.E., Ragozzine, D., Stansberry, J., Fraser, W.C., 2010. The size, density, and formation of the Orcus-Vanth system in the Kuiper belt. Astron. J. 139, 2700–2705.

Buratti, B.J., Hofgartner, J.D., Hicks, M.D., Weaver, H.A., Stern, S.A., Momary, T., Mosher, J.A., Beyer, R.A., Verbiscer, A.J., Zangari, A.M., Young, L.A., Lisse, C.M., Singer, K., Cheng, A., Grundy, W., Ennico, K., Olkin, C.B., 2017. Icarus 287, 207–217.

Delbo, M., Mueller, M., Emery, J.P., Rozitis, B., and Capria T.M., 2015, 'Asteroid thermophysical modeling' in Asteroids IV, Bottke, W.F., DeMeo, F.E., Michel, P. (Eds.), University of Arizona Press.

Essén, H., 2014. The physics of rotational flattening and the point core model. Int. J. Geosci. 5, 555–570.

Farinella, P., Milani, A., Nobili, A.M., Valsecchi, G.B., 1979. Tidal evolution and the Pluto-Charon system. Moon Planets 20, 415.

Fornasier, S., Lellouch, E., Müller, T., Santos-Sanz, P., Panuzzo, P., Kiss, C., Lim, T., Mommert, M., Bockelee-Morvan, D., Vilenius, E., Stansberry, J., Tozzi, G.P., Mottola, S., Delsanti, A., Crovisier, J., Duffard, R., Henry, F., Lacerda, P., Barucci, A., Gicquel, A., 2013. TNOs are cool: a survey of the trans-Neptunian region. VIII. Combined Herschel PACS and SPIRE observations of nine bright targets at 70–500 μm. Astron. Astrophys. 555, A15.

Fraser, W.C., Batygin, K., Brown, M.E., Bouchez, A., 2013. The mass, orbit, and tidal evolution of the Quaoar-Weywot system. Icarus 222, 357–363.

Goldreich, P., Soter, S., 1966. Q in the solar system. Icarus 5, 375–389.

Grundy, W.M., Noll, K.S., Virtanen, J., Muinonen, K., Kern, S.D., Stephens, D.C., Stansberry, J.A., Levison, H.F., Spencer, J.R., 2008. (42355) Typhon Echidna: scheduling observations for binary orbit determination. Icarus 197, 260–268.

Grundy, W.M., Noll, K.S., Nimmo, F., Roe, H.G., Buie, M.W., Porter, S.B., Benecchi, S.D., Stephens, D.C., Levison, H.F., Stansberry, J.A., 2011. Five new and three improved mutual orbits of Transneptunian binaries. Icarus 213, 678–692.

Grundy, W. M.; Binzel, R. P.; Buratti, B. J.; Cook, J. C.; Cruikshank, D. P.; Dalle Ore, C. M.; Earle, A. M.; Ennico, K.; Howett, C. J. A.; Lunsford, A. W.; Olkin, C. B.; Parker, A. H.; Philippe, S.; Protopapa, S.; Quirico, E.; Reuter, D. C.; Schmitt, B.; Singer, K. N.; Verbiscer, A. J.; Beyer, R. A.; Buie, M. W.; Cheng, A. F.; Jennings, D. E.; Linscott, I. R.; Parker, J. Wm.; Schenk, P. M.; Spencer, J. R.; Stansberry, J. A.; Stern, S. A.; Throop, H. B.; Tsang, C. C. C.; Weaver, H. A.; Weigle, G. E.; Young, L. A., 2016, Surface compositions across Pluto and Charon, Science, Volume 351, Issue 6279, id.aad9189.

Grundy, W.M., Noll, K.S., Buie, M.W., Benecchi, S.D., Ragozzine, D., Roe, H.G., 2018. The mutual orbit, mass, and density of Transneptunian binary G!kún‖'hòmdímà (229762 2007 UK$_{126}$). Icarus (in press).

Kiss, Csaba, Marton, Gábor, Farkas-Takács, Anikó, Stansberry, John, Müller, Thomas, Vinkó, József, Balog, Zoltán, Ortiz, Jose-Luis, Pál, András, 2017. Discovery of a satellite of the large trans-Neptunian object (225088) 2007 OR$_{10}$. Astrophys. J. Lett. 838, L1.

Kovalenko, I.D., Doressoundiram, A., Lellouch, E., Vilenius, E., Müller, T., Stansberry, J., 2017. "TNOs are cool": a survey of the trans-Neptunian region. XIII. Statistical analysis of multiple trans-Neptunian objects observed with Herschel space observatory. Astron. Astrophys. 608, A19.

Krist, J., Hook, R., Stoehr, F., 2010. Astrophysics Source Code Library, Record Ascl. (1010.057).

Lellouch, E., Stansberry, J., Emery, J., Grundy, W., Cruikshank, D.P., 2011. Thermal properties of Pluto's and Charon's surfaces from Spitzer observations. Icarus 214, 701–716.

Lellouch, E., Santos-Sanz, P., Lacerda, P., Mommert, M., Duffard, R., Ortiz, J.L., Müller, T.G., Fornasier, S., Stansberry, J., Kiss, C.S., Vilenius, E., Mueller, M., Peixinho, N., Moreno, R., Groussin, O., Delsanti, A., Harris, A.W., 2013. "TNOs are cool": a survey of the trans-Neptunian region. IX. Thermal properties of Kuiper Belt objects and centaurs from combined Herschel and Spitzer observations. Astron. Astrophys. 557, A60.

Lellouch, E., Santos-Sanz, P., Fornasier, S., Lim, T., Stansberry, J., Vilenius, E., Kiss, Cs., Müller, T., Marton, G., Protopapa, S., Panuzzo, P., Moreno, R., 2016. The long-wavelength thermal emission of the Pluto-Charon system from Herschel observations. Evidence for emissivity effects. Astron. Astrophys. 588, A2.

Lellouch, E.; Moreno, R.; Müller, T.; Fornasier, S.; Santos-Sanz, P.; Moullet, A.; Gurwell, M.; Stansberry, J.; Leiva, R.; Sicardy, B.; Butler, B.; Boissier, J., 2017, The thermal emission of centaurs and trans-Neptunian objects at millimeter wavelengths from ALMA observations, Astron. Astrophys., 608, A45.

Lupo, M.J., Lewis, J.S., 1979. Mass-radius relationships in icy satellites. Icarus 40, 157–170.

McKinnon, W.B., Durham, W.B., Stern, L.A., 2005. Cold compaction of porous ice, and the densities of Kuiper belt objects. In: Paper Presented at: Asteroids, Comets, and Meteors, Rio de Janeiro, Brazil, August 7–12, 2005.

McKinnon, W.B., Prialnik, D., Stern, S.A., Coradini, A., 2008. Structure and evolution of Kuiper Belt objects and dwarf planets. In: The Solar System beyond Neptune. University of Arizona Press.

Müller, T.G., et al., 2018, Icarus, (submitted).

Naoz, S., 2016. The eccentric Kozai-Lidov effect and its applications. Annu. Rev. Astron. Astrophys. 54, 441–489.

Nelder, J., Mead, R., 1965. A simplex method for function minimization. Comput. J. 7, 308–313.

Nicholson, P.D., Cuk, M., Sheppard, S.S., Nesvorny, D., Johnson, T.V., 2008. Irregular satellites of the giant planets. In: The Solar System beyond Neptune. University of Arizona Press.

Nimmo, F., Umurhan, O., Carey, M., Lisse, C.M., Bierson, C.J., Lauer, T.R., Marc, W., Buie, M.W., Throop, H.B., Kammer, J.A., Roberts, J.H., McKinnon, W.B., Zangarie, A.M., Moore, J.M., Stern, A.S., Young, L.A., Weaver, H.A., Olkin, C.B., Ennico, K., 2017. Mean radius and shape of Pluto and Charon from New Horizons images. Icarus 287, 12–29.

Noll, K.S., Grundy, W.M., Chiang, E.I., Margot, J.-L., Kern, S.D., 2008. Binaries in the Kuiper Belt. In: The Solar System beyond Neptune. University of Arizona Press.

Ortiz, J.L., Santos-Sanz, P., Sicardy, B., Benedetti-Rossi, G., Berard, D., Morales, N., Duffard, R., Braga-Ribas, F., Hopp, U., Ries, C., Nascimbeni, V., Marzari, F., Granata, V., Pál, A., Kiss, C., Pribulla, T., Komžík, R., Hornoch, K., Pravec, P., Bacci, P., Maestripieri, M., Nerli, L., Mazzei, L., Bachini, M., Martinelli, F., Succi, G., Ciabattari, F., Mikuz, H., Carbognani, A., Gaehrken, B., Mottola, S., Hellmich, S., Rommel, F.L., Fernández-Valenzuela, E., Campo Bagatin, A., Cikota, S., Cikota, A., Lecacheux, J., Vieira-Martins, R., Camargo, J.I.B., Assafin, M., Colas, F., Behrend, R., Desmars, J., Meza, E., Alvarez-Candal, A., Beisker, W., Gomes-Junior, A.R., Morgado, B.E., Roques, F., Vachier, F., Berthier, J., Mueller, T.G., Madiedo, J.M., Unsalan, O., Sonbas, E., Karaman, N., Erece, O., Koseoglu, D.T., Ozisik, T., Kalkan, S., Guney, Y.,

Niaei, M.S., Satir, O., Yesilyaprak, C., Puskullu, C., Kabas, A., Demircan, O., Alikakos, J., Charmandaris, V., Leto, G., Ohlert, J., Christille, J.M., Szakáts, R., Takácsné Farkas, A., Varga-Verebélyi, E., Marton, G., Marciniak, A., Bartczak, P., Santana-Ros, T., Butkiewicz-Bak, M., Dudzinski, G., Alì-Lagoa, V., Gazeas, K., Tzouganatos, L., Paschalis, N., Tsamis, V., Sánchez-Lavega, A., Pérez-Hoyos, S., Hueso, R., Guirado, J.C., Peris, V., Iglesias-Marzoa, R., 2017. The size, shape, density and ring of the dwarf planet Haumea from a stellar occultation. Nature 550, 219–223.

Pál, A., Kiss, Cs., Müller, Th.G., Molnár, L., Szabó, R., Szabó, Gy.M., Sárneczky, K., Kiss, L.L., 2016. Large size and slow rotation of the trans-Neptunian object (225088) 2007 OR$_{10}$ discovered from Herschel and K2 observations. Astron. J. 151, 117 aid.

Perets, H.B., Naoz, S., 2009. Kozai cycles, tidal friction, and the dynamical evolution of binary minor planets. Astrophys. J. Lett. 699, L17–L21.

Plummer, H.C., 1919. On the ellipticities of the Maclaurin ellipsoids. Mon. Not. R. Astron. Soc. 80, 26–33.

Press, W.H., Teukolsky, S.A., Vetterling, W.T., Flannery, B.P., 1992. Numerical Recipes in C. Cambridge University Press, New York.

Ragozzine, D., Brown, M.E., 2009. Orbits and masses of the satellites of the dwarf planet Haumea = 2003 EL$_{61}$. Astrophys. J. 137, 4766–4776.

Sahu, K., Deustua, K., Sabbi, E., 2017. WFC3/UVIS Photometric Transformations, WFC3 Instrument Science Report. STScI.

Stern, S. A.; Bagenal, F.; Ennico, K.; Gladstone, G. R.; Grundy, W. M.; McKinnon, W. B.; Moore, J. M.; Olkin, C. B.; Spencer, J. R.; Weaver, H. A.; Young, L. A.; Andert, T.; Andrews, J.; Banks, M.; Bauer, B.; Bauman, J.; Barnouin, O. S.; Bedini, P.; Beisser, K.; Beyer, R. A.; Bhaskaran, S.; Binzel, R. P.; Birath, E.; Bird, M.; Bogan, D. J.; Bowman, A.; Bray, V. J.; Brozovic, M.; Bryan, C.; Buckley, M. R.; Buie, M. W.; Buratti, B. J.; Bushman, S. S.; Calloway, A.; Carcich, B.; Cheng, A. F.; Conard, S.; Conrad, C. A.; Cook, J. C.; Cruikshank, D. P.; Custodio, O. S.; Dalle Ore, C. M.; Deboy, C.; Dischner, Z. J. B.; Dumont, P.; Earle, A. M.; Elliott, H. A.; Ercol, J.; Ernst, C. M.; Finley, T.; Flanigan, S. H.; Fountain, G.; Freeze, M. J.; Greathouse, T.; Green, J. L.; Guo, Y.; Hahn, M.; Hamilton, D. P.; Hamilton, S. A.; Hanley, J.; Harch, A.; Hart, H. M.; Hersman, C. B.; Hill, A.; Hill, M. E.; Hinson, D. P.; Holdridge, M. E.; Horanyi, M.; Howard, A. D.; Howett, C. J. A.; Jackman, C.; Jacobson, R. A.; Jennings, D. E.; Kammer, J. A.; Kang, H. K.; Kaufmann, D. E.; Kollmann, P.; Krimigis, S. M.; Kusnierkiewicz, D.; Lauer, T. R.; Lee, J. E.; Lindstrom, K. L.; Linscott, I. R.; Lisse, C. M. ; Lunsford, A. W.; Mallder, V. A.; Martin, N.; McComas, D. J.; McNutt, R. L.; Mehoke, D.; Mehoke, T.; Melin, E. D.; Mutchler, M.; Nelson, D.; Nimmo, F.; Nunez, J. I.; Ocampo, A.; Owen, W. M.; Paetzold, M.; Page, B.; Parker, A. H.; Parker, J. W.; Pelletier, F.; Peterson, J.; Pinkine, N.; Piquette, M.; Porter, S. B.; Protopapa, S.; Redfern, J.; Reitsema, H. J.; Reuter, D. C.; Roberts, J. H.; Robbins, S. J.; Rogers, G.; Rose, D.; Runyon, K.; Retherford, K. D.; Ryschkewitsch, M. G.; Schenk, P.; Schindhelm, E.; Sepan, B.; Showalter, M. R.; Singer, K. N.; Soluri, M.; Stanbridge, D.; Steffl, A. J.; Strobel, D. F.; Stryk, T.; Summers, M. E.; Szalay, J. R.; Tapley, M.; Taylor, A.; Taylor, H.; Throop, H. B.; Tsang, C. C. C.; Tyler, G. L.; Umurhan, O. M.; Verbiscer, A. J.; Versteeg, M. H.; Vincent, M.; Webbert, R.; Weidner, S.; Weigle, G. E.; White, O. L.; Whittenburg, K.; Williams, B. G.; Williams, K.; Williams, S.; Woods, W. W.; Zangari, A. M.; Zirnstein, E., 2015, The Pluto system: initial results from its exploration by New Horizons, Science, Volume 350, Issue 6258, id.aad1815.

Thirouin, A., Noll, K.S., Ortiz, J.-L., Morales, N., 2014. Rotational properties of the binary and non-binary populations in the trans-Neptunian belt. Astron. Astrophys. 569, A3.

Weaver, H. A.; Buie, M. W.; Buratti, B. J.; Grundy, W. M.; Lauer, T. R.; Olkin, C. B.; Parker, A. H.; Porter, S. B.; Showalter, M. R.; Spencer, J. R.; Stern, S. A.; Verbiscer, A. J.; McKinnon, W. B.; Moore, J. M.; Robbins, S. J.; Schenk, P.; Singer, K. N.; Barnouin, O. S.; Cheng, A. F.; Ernst, C. M.; Lisse, C. M.; Jennings, D. E.; Lunsford, A. W.; Reuter, D. C.; Hamilton, D. P.; Kaufmann, D. E.; Ennico, K.; Young, L. A.; Beyer, R. A.; Binzel, R. P.; Bray, V. J.; Chaikin, A. L.; Cook, J. C.; Cruikshank, D.P.; Dalle Ore, C. M.; Earle, A. M.; Gladstone, G. R.; Howett, C. J. A.; Linscott, I. R.; Nimmo, F.; Parker, J. Wm.; Philippe, S.; Protopapa, S.; Reitsema, H. J.; Schmitt, B.; Stryk, T.; Summers, M. E.; Tsang, C. C. C.; Throop, H. H. B.; White, O. L.; Zangari, A. M., 2016, Science, Volume 351, Issue 6279, id.aae0030.